

All-Solution-Processed Top-Emitting InP Quantum Dot Light-Emitting Diode with Polyethylenimine Interfacial Layer

Youngwoo Jeon, Soobin Sim, Doyoon Shin, Wan Ki Bae, Hyunkoo Lee,* and Hyunho Lee*

Recent studies on top-emitting structure, which is designed to enhance the color purity and outcoupling efficiency of quantum-dot light-emitting diodes (QLEDs), employ commercially unviable methods owing to limited options for applying the hole injection layer through solution processes on the bottom electrode. In this study, all-solution-processable conventional top-emitting QLEDs (TQLEDs) are successfully fabricated by introducing a polyethylenimine (PEI) interlayer, doping isopropyl alcohol (IPA) into the hole-injection layer (poly(3,4-ethylenedioxythiophene): poly(4-styrenesulfonate), PEDOT:PSS), and using the dynamic spin-coating method. The increased hole injection resulting from the tuned anode-HIL interface by the PEI and IPA-doped HIL, coupled with the enhanced outcoupling efficiency and full width at half maximum (FWHM) derived from the optimized cavity length through simulation, realizes a red InP QLED with high efficiency and color purity. The optimized TQLED exhibits a maximum current efficiency and FWHM of 28.04 cd A^{-1} and 36 nm, respectively, which are threefold higher and 8 nm narrower than those of bottom-emitting QLEDs, marking the highest current efficiency ever reported for top-emitting red InP QLEDs.

1. Introduction

Quantum dot light-emitting diodes (QLEDs) are emerging as next-generation light sources, presenting advantageous features such as size-controlled tunable emission wavelength, ease of solution processing, and a narrow full width at half maximum (FWHM). Most importantly, the energy bandgap and emission wavelength can be tuned by simply adjusting the core size through the quantum confinement effect is beneficial for implementing a diverse color spectrum in displays.^[1–4] Among various quantum dot (QD) materials, InP QD have a suitable bulk bandgap (1.35 eV) and a large excitonic Bohr radius ($\approx 10 \text{ nm}$), presenting eco-friendly attributes distinct from those of Cd-based QDs.^[5,6] Recently reported red-, green-, and blue-emission InP QLEDs have demonstrated maximum external quantum efficiency (EQE) values of 22.56%, 16.3%, and 2.8%, respectively.^[7–9]

Regarding the structure of emerging LEDs such as organic light-emitting diodes (OLEDs) and QLEDs, the

bottom-emitting structure is widely used in commercialized large-area displays today.^[10] In bottom-emitting structure, the light generated in the emission layer (EML) exits through the glass substrate, and the light outcoupling mechanisms are as follows: The light generated from the EML passes through the constituent layers, transparent electrodes such as indium tin oxide (ITO), and glass substrate as it exits, losing some light in the process.^[11,12] The light extracted from the substrate is partially blinded by the thin-film transistor (TFT, for driving the LED) connected to the pixels, further increasing the loss of light.^[13,14] The light eventually decreases to 30% or less than that, generated in the EML.^[13–16] These losses in the light-extraction process of bottom-emitting structures critically limit the application of mobile displays that demand high resolution and luminance.^[10] In contrast, in a top-emitting structure, the light generated from the EML passes through the semi-transparent top electrode. Compared to the bottom-emitting structure, the top-emitting structure has significant advantages in terms of the aperture ratio and light extraction because the light generated in the EML escapes directly without passing through the glass substrate or TFT. Moreover, it offers facile control of the microcavity effect.^[15] In the top-emitting structure, the light generated in the EML is

Y. Jeon, H. Lee
Department of Electronic Engineering
Kwangjuon University
Seoul 01897, Republic of Korea
E-mail: hyunho@kw.ac.kr

S. Sim, H. Lee
Department of Electrical Engineering and Institute
of Advanced Materials and Systems
Sookmyung Women's University
Seoul 04310, Republic of Korea
E-mail: lhk108@sookmyung.ac.kr

D. Shin, W. K. Bae
SKKU Advanced Institute of Nanotechnology (SAINT)
Sungkyunkwan University
Suwon 16419, Republic of Korea

 The ORCID identification number(s) for the author(s) of this article can be found under <https://doi.org/10.1002/aelm.202400195>

© 2024 The Author(s). Advanced Electronic Materials published by Wiley-VCH GmbH. This is an open access article under the terms of the [Creative Commons Attribution](https://creativecommons.org/licenses/by/4.0/) License, which permits use, distribution and reproduction in any medium, provided the original work is properly cited.

DOI: 10.1002/aelm.202400195

reflected off the reflective bottom electrode and semitransparent top electrode, causing interference. During the process, the cavity length can be optimized by controlling the thickness of the constituent layers, such as the hole transport layer (HTL) and electron transport layer (ETL).^[17–19] The optimized cavity length induces constructive interference between the reflected light and the light generated in the EML, resulting in a reduction in the FWHM and an increase in luminance in the normal direction. Based on these characteristics, a top-emitting structure is appropriate for AR/VR and mobile display applications.^[10,19,20]

In a top-emitting structure, the bottom electrode requires high conductivity to inject charges for device operation and high reflectivity to reflect light directed toward the bottom side to the top semi-transparent electrode. Therefore, Ag, owing to its high conductivity and reflectivity in the visible light range, is widely used as the bottom electrode in top-emitting LEDs.^[21] Most studies on top-emitting QLEDs (TQLEDs) have been conducted based on an inverted structure using a Ag cathode as the bottom electrode. However, in an inverted structure, where the ETL is deposited on the bottom cathode, the scarcity of HTL candidates that allow solution processability is a constraint. Most materials commonly used as HTL, including 4,4'-bis(9-carbazolyl)-2,2'-biphenyl (CBP), tris(4-carbazoyl-9-ylphenyl)amine (TCTA), and poly[(9,9-dioctylfluorenyl-2,7-diyl)-co-(4,4'-(N-(4-sec-butylphenyl)diphenylamine)] (TFB), utilize non-polar and hydrophobic solvents such as chlorobenzene and toluene. When these solvents make contact with the QD layer, the photoluminescence (PL) intensity of QDs degrade, and they are washed away.^[22] Therefore, in current inverted TQLEDs, the HTL and hole injection layer (HIL) are typically deposited via thermal evaporation under high-vacuum condition. However, the use of a high-vacuum process in device fabrication significantly diminishes the ease of solution processing for QLEDs.^[23,24] Furthermore, in the circuit design stage for commercialization, where pixels are connected with the TFT, an inverted LED requires additional negative gate signals to be applied to the data line to drive the pixels. Consequently, the circuitry and operational conditions are more complex than those of conventional LEDs. Therefore, top-emitting OLEDs used in mobile displays have a conventional structure, to easily generate gate signals with a common anode.^[25,26]

Studies on all-solution-processable TQLEDs with a conventional structure are few owing to the difficulty of using Ag as the bottom anode. To achieve highly efficient QLEDs, it is crucial for the HIL and HTL to inject and transport holes from the anode to the QD-emission layer. Commonly used HILs in conventional bottom-emitting QLEDs (BQLEDs), such as poly(3,4-ethylenedioxythiophene):poly(4-styrenesulfonate) (PEDOT:PSS) and NiO_x, are hydrophilic and have high surface tension.^[27,28] In BQLEDs, the surface tension of the anode, such as ITO and indium zinc oxide (IZO), can be reduced via ultraviolet (UV)-ozone treatment, facilitating the deposition of a hydrophilic HIL through a solution process.^[29] However, metals such as Ag undergo oxidation or damage owing to the oxygen, oxides, and ozone generated during the UV-ozone treatment.^[30,31] Therefore, depositing a hydrophilic HIL onto Ag using UV-ozone treatment is infeasible. A few reports have addressed this problem using multiple bottom electrodes in conventional TQLED fabrication and stacking additional transparent electrodes, such as ITO

and IZO, on the bottom reflective Ag anode, forming an anode structure (such as ITO/Ag/ITO and IZO/Ag/IZO).^[18,32–35] The structure can feasibly deposit a hydrophilic HIL through a solution process via UV-ozone treatment at the transparent electrode stacked on top of the Ag. However, in this structure, ITO, which has a higher sheet resistance than pure metals like Ag and Al, contacts the HIL and adversely affects the conductivity of the device.^[36] Moreover, unlike thermally evaporated metals, ITO is sputter deposited in high-temperature and vacuum environments, incurring additional fabrication costs.^[37–41]

In this study, we successfully fabricated all-solution-processable TQLEDs with a conventional structure comprising a single Ag anode. Introduction of polyethylenimine (PEI) interlayer, and the doping of isopropyl alcohol (IPA) into PEDOT:PSS significantly improved the wettability of PEDOT:PSS on the Ag anode. Additionally, a uniform anode-HIL film was formed by depositing doped PEDOT:PSS using the dynamic spin-coating method. Furthermore, the tuned work function and bent energy levels at the interface between the PEI interlayer and IPA-doped PEDOT:PSS significantly improved the hole injection from the anode-HIL to the QD layer compared to that of BQLEDs. Following the optimization of the cavity through optical simulation, the optimized device showed a current efficiency of 28.04 cd A⁻¹, which is the highest result ever reported for top-emitting InP red QLEDs, with an improved color purity that is 8 nm narrower than that of BQLEDs.

2. Results and Discussion

2.1. Configuration of Bottom Electrode with HIL

The main objective in fabricating all-solution-processable conventional TQLEDs is the conformal coating of the HIL on the Ag anode. We introduced three techniques for depositing PEDOT:PSS, a hydrophilic HIL, onto an Ag anode.

2.1.1. Introduction of PEI Interlayer

PEI, a polymer containing an aliphatic amine, is widely used in various optoelectronics devices owing to its notable electrochemical characteristics, such as tunable work function, stability, amphiphilic properties, and good physisorption to electrodes.^[42] In particular, amphiphilic PEI, which can be dissolved in both hydrophilic and hydrophobic solvents, was introduced to improve the uniformity of the film at various interfaces, such as the ETL, HTL, or EML.^[43–45] We introduced PEI onto the Ag anode as a buffer layer and sequentially spin-coated it with the hydrophilic HIL, PEDOT:PSS. An atomic force microscopy (AFM) image of the glass/Ag/PEI film (**Figure 1a**) shows a root-mean-square roughness (R_q) of 5.26 nm, indicating a rougher surface compared to the 1.56 nm glass/Ag film (**Figure S1a**, Supporting Information). PEI exhibits island growth when it is very thin (<11 nm); therefore, it can be considered that PEI has firmly formed on the Ag anode.^[46,47] The island-formed PEI thin films increase the interfacial area, which is predicted to improve the wettability of PEDOT:PSS on the Ag anode. **Figure 1d** shows the contact angle of the PEDOT:PSS on the Ag surface. The

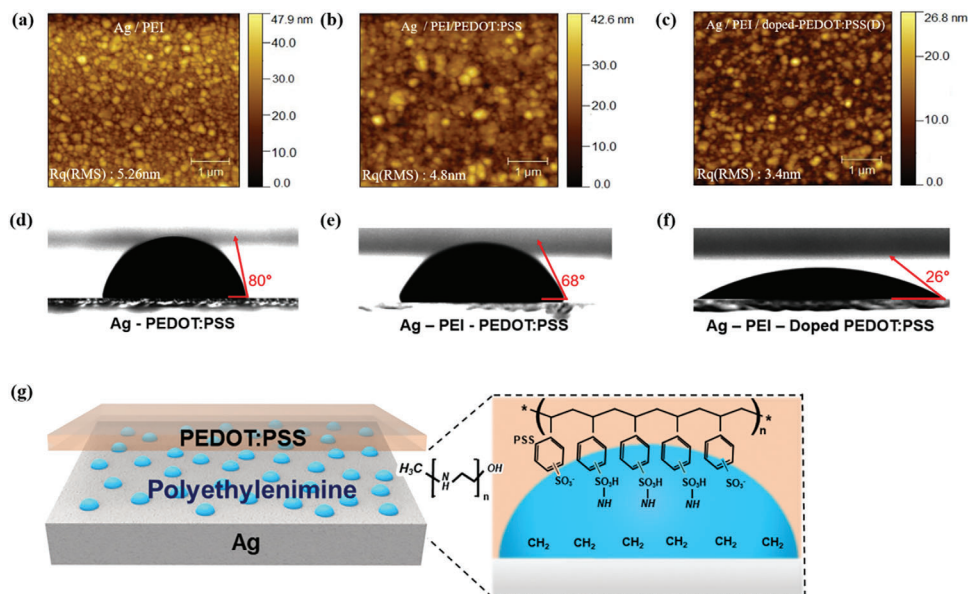


Figure 1. Film characteristic of the anode (Ag) and hole injection layer (PEDOT:PSS). AFM image of a) Ag/PEI, b) Ag/PEI/PEDOT:PSS, and c) Ag/PEI/doped-PEDOT:PSS using dynamic spin-coating. Contact angles of d) Ag/PEDOT:PSS, e) Ag/PEI/PEDOT:PSS, and f) Ag/PEI/doped-PEDOT:PSS. g) Schematic of film formation at the anode/HIL interface.

measured contact angle was $\approx 80^\circ$, indicating that the polarity difference between Ag and PEDOT:PSS caused a wettability problem. The direct deposition of PEDOT:PSS onto Ag was attempted using the spin-coating method. However, as expected from the contact angle measurements, PEDOT:PSS did not form on the Ag (Figure S2a, Supporting Information). The Ag/PEI/PEDOT:PSS film exhibited an R_q of 4.8 nm, as shown in Figure 1b. Although the surface was rough, the introduction of PEI enabled the successful deposition of PEDOT:PSS on Ag (Figure S2b, Supporting Information) because of improved wettability. The contact angle of PEDOT:PSS on the Ag/PEI film reduced to 68° (Figure 1e), confirming the role of PEI in increasing the wettability, which is attributed to its chemical structure. As shown in Figure 1g, the amine groups (NH) of PEI react with the SO_3H of PSS to form a solid polymer blend.^[48–50] At the interfaces of PEDOT:PSS and PEI, they undergo crosslinking with each other, resulting in the formation of a stable film.^[51,52] Moreover, hydrocarbon groups (such as CH_2) face the Ag interface, indicating good adherence to the anode.

2.1.2. Surface Tension of PEDOT:PSS

Although the introduction of the PEI interlayer enabled the successful formation of the PEDOT:PSS film on the Ag anode, the contact angle (68°) and R_q (4.8 nm) of the film remained relatively high, indicating its unsuitability for device applications. The roughness of the PEDOT:PSS film originates from the water solvent, which has high surface tension.^[27] Therefore, we doped organic solvent into the hydrophilic polymer, PEDOT:PSS. Doping of organic solvents such as dimethyl sulfoxide (DMSO) and IPA into PEDOT:PSS was performed to enhance the conductivity of PEDOT:PSS.^[53,54] Moreover, such as IPA and ethanol, which have a hydrophobic nature, can enhance the film wettability on

hydrophobic surfaces like SiO_2 or graphene.^[55–57] In particular, when IPA was doped into PEDOT:PSS, the OH groups of IPA formed hydrogen bonds with the SO_3^- groups of PSS.^[58] This enhanced the conductivity of PEDOT:PSS and improved the contact angle and film uniformity.^[59–61] Figure 1f shows the contact angle of the IPA-doped PEDOT:PSS (hereafter referred to as doped-PEDOT:PSS) on the Ag/PEI film. The contact angle is $\approx 26^\circ$, which is 42° lower than that of pristine PEDOT:PSS. However, the real image of the doped-PEDOT:PSS film on the Ag/PEI film (Figure S2c, Supporting Information) shows hazy patterns on the surface, clearly indicating that the surface of the PEDOT:PSS film is unsuitable for device applications and needs further improvement.

2.1.3. Uniform Film Morphology of HIL with Dynamic Spin-Coating

The surface roughness of the PEDOT:PSS directly spin-coated on the UV-ozone-treated glass is ≈ 2.96 nm (Figure S1b, Supporting Information). Thus, for functional device applications, the surface roughness of the PEDOT:PSS films should be within 3–4 nm. As shown in Figure S2b,c (Supporting Information), a coffee-ring-like hazy pattern is observed in the spin-coated PEDOT:PSS and doped-PEDOT:PSS films. During static spin-coating, PEI, which dissolves in low-pH water, is partially dissolved by PEDOT:PSS solution with pH values ranging from 1.2 to 2.2.^[62,63] Additionally, PEI is soluble in IPA, which affects and damages Ag/PEI films.^[64] Therefore, we introduced a dynamic spin-coating method to further reduce the roughness of PEDOT:PSS films. In dynamic spin coating, the substrate is pre-spun at a certain speed, and the solution is then dispensed onto the rotating substrate. This differs from static spin-coating, in which the solution is applied to the substrate before rotating it. Dynamic spin-coating enhances the uniformity of films with

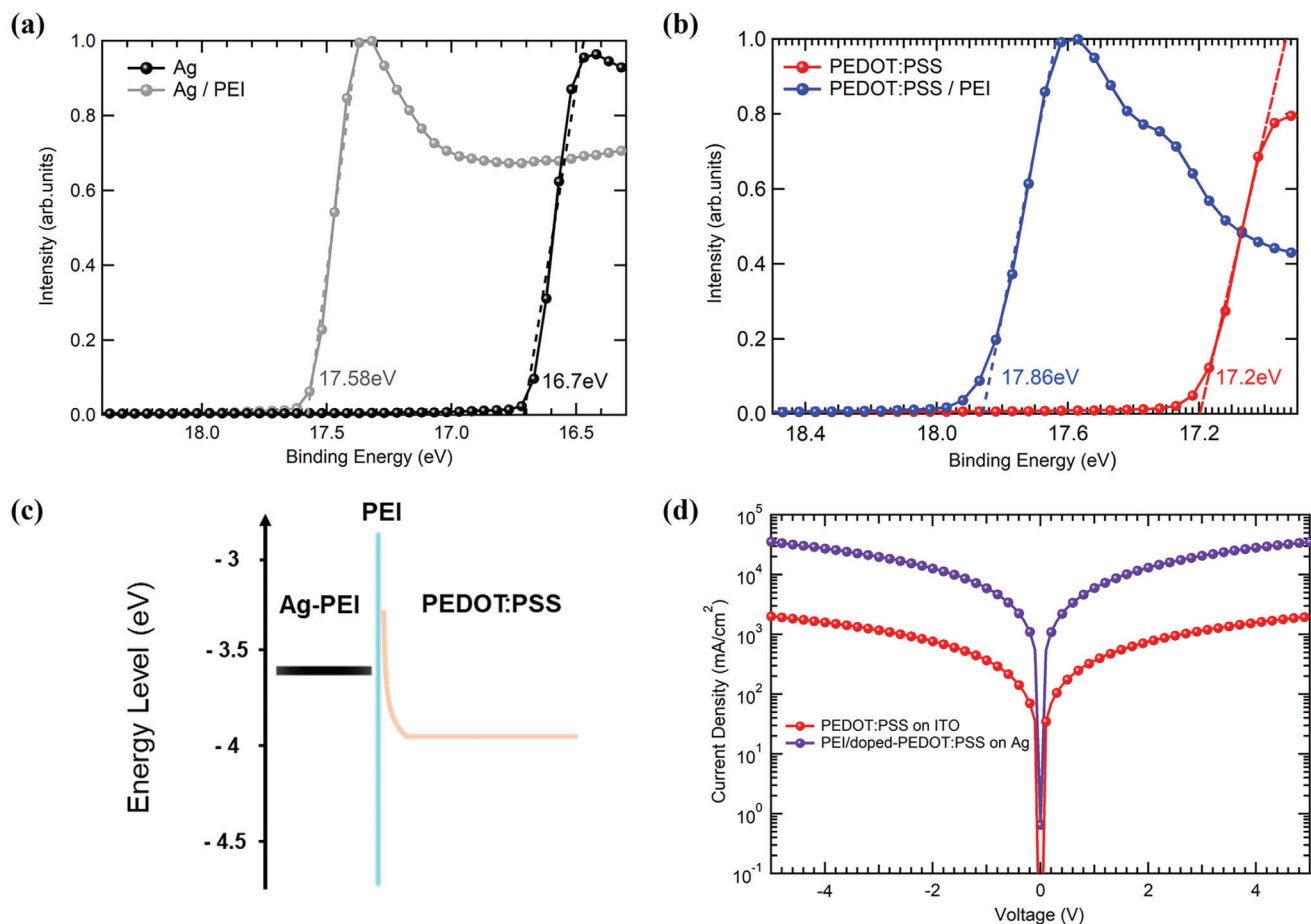


Figure 2. UPS spectra of a) Ag and Ag/PEI and b) doped-PEDOT:PSS and doped -PEDOT:PSS/PEI. c) Energy level alignment at the Ag/PEI/doped-PEDOT:PSS interface. d) J–V characteristic of the hole only device (PEDOT:PSS on ITO (red line) and PEI/doped-PEDOT:PSS on Ag (purple line)).

poor wettability and greatly reduces the solvent residence time on the film, thereby effectively minimizing damage to the film.^[65,66] The image of the Ag/PEI/doped-PEDOT:PSS film deposited using the dynamic spin-coating method (Figure S2d, Supporting Information) confirmed that the film did not exhibit coffee-ring-like hazy pattern. The AFM image of the dynamically-spin coated PEI/doped-PEDOT:PSS film on the Ag anode (Figure 1c) exhibits a uniform film formation with an R_q of 3.4 nm. The roughness difference was only ≈ 0.44 nm compared to the roughness of PEDOT:PSS statically spin-coated on UV-ozone-treated glass (Figure S1b, Supporting Information). Furthermore, to confirm the impact of the solvent type used for doping PEDOT:PSS on film formation, we compared films utilizing PEDOT:PSS doped with either methanol or ethanol (Figure S2e,f, Supporting Information). When using PEDOT:PSS doped with ethanol or methanol, a hazy pattern and cloudy surface were observed, unlike IPA.

2.2. Electrical Characteristics of the Anode Composition

Through the introduction of a PEI interlayer and dynamic spin-coating of IPA doped- PEDOT:PSS, uniform coating of PEI-

DOT:PSS onto the Ag anode was successfully achieved. However, even if PEDOT:PSS is uniformly formed on the Ag anode, facile hole injection through the films cannot be guaranteed. Therefore, the hole-injection properties of these films need to be investigated. The energetic influence of PEI on the Ag-doped PEDOT:PSS interface was investigated using ultraviolet photoelectron spectroscopy (UPS) (Figure 2a,b; Figure S3, Supporting Information). When PEI is in a thin-film state (<10 nm), it functions as a surface modifier rather than insulator by establishing strong interfaces and/or molecular dipoles, reducing the work function at the material interface.^[42,67] As shown in Figure 2a,b, the work functions of Ag and doped-PEDOT:PSS (calculated by $WF = 21.2 \text{ eV} - E_{\text{cutoff}}$) decreased from 4.5 to 3.62 eV and from 4.0 to 3.34 eV, respectively, upon the insertion of PEI. The analysis of the work function indicates that the Ag/PEI/doped-PEDOT:PSS structure shows different properties at the interface compared to the conventional ITO/PEDOT:PSS structure in terms of energy levels. Generally, a work function difference of at least +0.3 eV is noted when holes are injected from ITO (4.7 eV) to PEDOT:PSS (5.0 eV).^[68–71] However, doped-PEDOT:PSS exhibits a significantly lower work function of 4.0 eV compared to the undoped PEDOT:PSS, which is attributed to the doping effect of IPA,^[72] and is even 0.5 eV lower than the

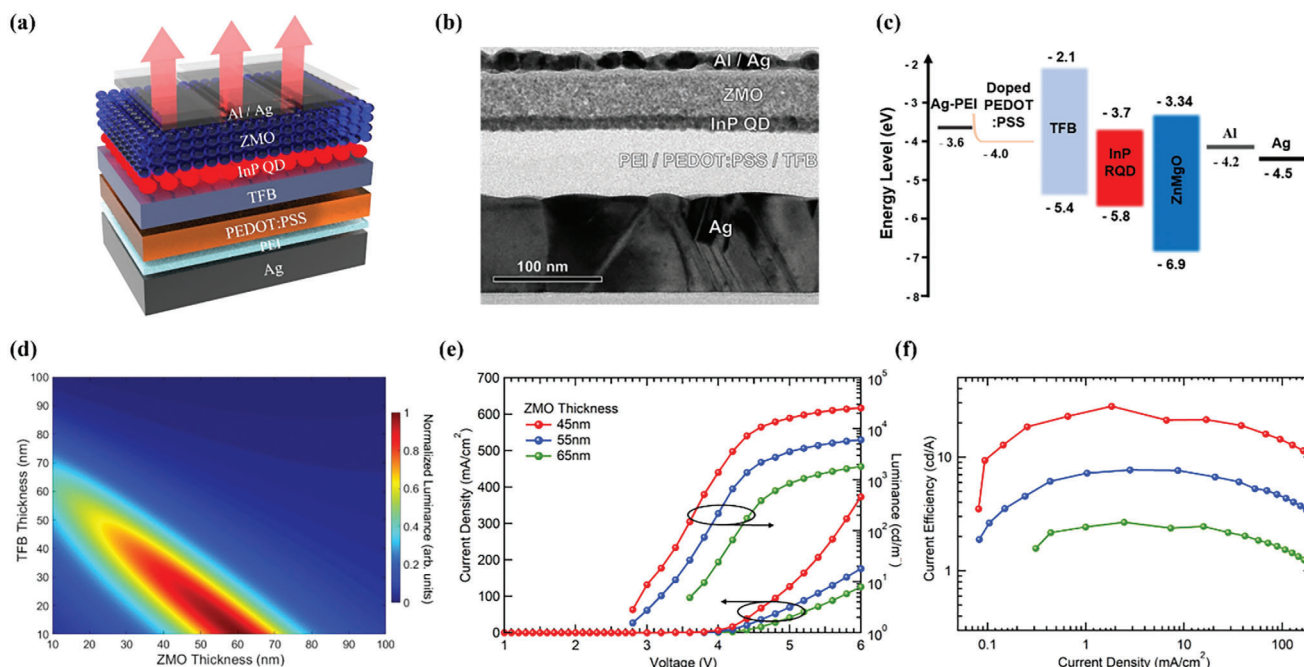


Figure 3. EL Characteristic of TQLEDs. a) Device structure. b) Cross-sectional TEM image of TQLEDs. c) Energy level distribution of TQLEDs. d) Calculated normalized luminance of TQLEDs based on HTL and ETL thickness using commercial optical simulation software (SETFOS). e) J - V - L characteristics of TQLEDs and f) current efficiency of TQLEDs with different ZMO thicknesses.

work function of Ag (4.5 eV). Furthermore, owing to the PEI interfacial layer, the work functions of Ag and doped-PEDOT:PSS at the interface shifted up toward the vacuum level, measuring 3.62 and 3.34 eV, respectively. Therefore, the energy-level barrier that the holes injected through the Ag anode need to overcome to reach the doped-PEDOT:PSS decreased from 0.5 to 0.28 eV. Subsequently, the holes that reached the PEI/doped-PEDOT:PSS interface moved smoothly along the bent energy band to the doped-PEDOT:PSS/HTL interface. The energy level alignment at the anode/HIL composition is shown in Figure 2c. A hole-only device (Anode/PEDOT:PSS/MoO₃/Al) was fabricated to investigate the hole-injection characteristics of the anode. Figure 2d shows the J - V characteristics of the hole-only devices with bottom- and top-emitting device anode compositions. In the forward-biased region (Ag anode), PEI/doped-PEDOT:PSS on Ag (purple line) exhibits significantly better hole injection properties than PEDOT:PSS on ITO (red line). At 5 V, PEI/doped-PEDOT:PSS on Ag exhibits a 17.6-fold increase in current density compared with PEDOT:PSS on ITO. The enhanced hole injection originated from the effective work function tuning at the anode composition, enabling holes to move smoothly along the bent energy band at the anode/HIL interface. The changes in hole injection properties at different IPA concentrations added to PEDOT:PSS were investigated using hole-only devices (Figure S4, Supporting Information). The current density increased until the IPA concentration reached 400% of the PEDOT:PSS (1:4 volume ratio). Furthermore, to compare hole injection with electron injection, we also fabricated an electron-only device. From Figure S4 (Supporting Information), it can be determined that the charge balance is optimized when the PEDOT:PSS:IPA ratio is near 2:1. Subsequently, based on the optimization of the device efficiency in the

electroluminescence (EL) device fabrication process, a final ratio of 2:1 (PEDOT:PSS:IPA) was adopted for device fabrication (Figure S5a,b, Supporting Information).

2.3. Electroluminescence Characteristics

Figure 3a illustrates the structure of fabricated TQLEDs. The bottom anode and a HIL are composed of Ag (100 nm)/PEI/doped-PEDOT:PSS (40 nm). Solution-processed TFB (22 nm), InP QD (12 nm), and ZnMgO (ZMO, 45 nm) were sequentially deposited on the HIL. Al (2 nm) was deposited to improve the contact between the ZMO and the transparent Ag cathode (15 nm). The multilayer structure of the TQLED can be observed in the cross-sectional transmission electron microscopy (TEM) image shown in Figure 3b. In Figure 3b, the island-form architecture of PEI is not observed at the interface between the Ag anode and the organic layer. This is because PEI, which has a low melting point (<70 °C),^[73] mixes with PEDOT:PSS during the annealing process of functional layers such as PEDOT:PSS and TFB (≈140 °C). As a result, PEI no longer maintains its island form and exists instead as a single film. The energy level distribution of each functional layer is shown in Figure 3c. A hole injection barrier is present at the interface between the doped-PEDOT:PSS and the TFB because of the energy level difference. Therefore, the charge injection balance in the QD layer should be carefully investigated by varying the electrical transport characteristics of each charge transport layer (TFB and ZMO). The microcavity effect could be determined by modifying the cavity lengths of the transport layers. The electrical and optical properties of the charge transport layers were simultaneously controlled by adjusting the thickness

Table 1. EL characteristics of TQLEDs with different ZMO thicknesses. EQE* was calculated considering the angle distribution properties (Figure 4a) by following the procedure in Part S1, Supporting Information.

ZMO [nm]	CE _{max} [cd A ⁻¹]	EQE* _{max} [%]	PE _{max} [cd W ⁻¹]	EL _{peak} [nm]	FWHM [nm]	CIE (X,Y)
45 nm	28.04	15.96	7.38	633	36	(0.694, 0.306)
55 nm	7.73	12.53	1.93	648	49	(0.705, 0.294)
65 nm	2.68	4.75	0.7	642	46	(0.7, 0.299)

of each transport layer. Calculating constructive and destructive interference based on the cavity length is imperative for controlling the microcavity effect, especially concerning optical properties. Figure 3d shows the calculated normalized luminance of the device as a function of the thickness of the charge transport layers using commercial optical simulation software (SETFOS). Based on the simulation results, the optimal thickness for the charge transport layers to enhance the optical performance could be estimated. Considering the simulation results with the thickness of the HTL (TFB, 22 nm) used in our previous study,^[74] the optimal thickness for the ETL (ZMO), which yielded the highest light extraction efficiency, was calculated to be ≈45 nm (Figure S6, Supporting Information). Figure 3e shows the *J-V-L* characteristics of the device in the normal direction at various ZMO thicknesses (45, 55, and 65 nm). As the ZMO thickness increases, the current density decreases. This can be attributed to the reduced injection of electrons, leading to an imbalance in charge injection between the holes and electrons.^[75] Furthermore, the microcavity effect significantly governs light extraction through the device. Based on the simulation results (Figure 3d), the device with 45 nm-ZMO exhibits optimized light extraction, resulting in a maximum luminance of 25 606 cd m⁻². As shown in Figure 3f, the device with 45 nm-ZMO exhibits a peak current efficiency of 28.04 cd A⁻¹. This value surpassed the current efficiency of the BQLED (Figure S7, Supporting Information) by more than three times, representing the highest efficiency ever reported for top-emitting InP QD-based QLED (Figure S8 and Table S1, Supporting Information). The reliability of our device is verified by the statistical distribution of the TQLEDs shown in Figure S9 (Supporting Information). The average current efficiency for the 48 devices was 18.86 cd A⁻¹ with a standard deviation of 5.08. When the thickness of ZMO increased to 55 and 65 nm, both maximum luminance and current efficiency decreased, with peak current efficiencies recorded at 7.73 and 2.68 cd A⁻¹, respectively.

The EL characteristics based on the ZMO thickness are summarized in Table 1. The measured power efficiency is ≈7.38 cd W⁻¹, which is twice the 3.18 cd W⁻¹ of BQLED. Furthermore, it surpasses the power efficiencies of Samsung's inkjet-printed RGB OLED displays (3.2 cd W⁻¹) and state-of-the-art prototype RGB QD-EL displays (3.5 cd W⁻¹) by more than twofold.^[76] To confirm the impact of PEI on the device, we investigated the EL characteristics of the devices with and without PEI (Figure S10, Supporting Information). In the case of the device without PEI (grey line), unstable device operation characteristics, such as off-axis points in the *J-V* curve are observed. This can be attributed to the rough surface in the absence of PEI, confirming that PEI plays a key role in forming a uniform PEDOT:PSS film. Unstable device operation was observed until the thickness of PEI was below 5 nm (0.5 mg mL⁻¹); furthermore, increasing the thickness

of PEI beyond 5 nm resulted in a decrease in EL performance (Figure S11, Supporting Information), so we utilize a PEI thickness of 5 nm. The lifetimes of the operating devices were also measured. The time needed for the initial luminance of the device to decrease by 75% (*T*₇₅) in the range of 1000–5000 cd m⁻² is 1.19 to 0.112 h. Based on this, the calculated acceleration factor (*n*) for our TQLEDs is ≈1.55,^[77,78] and the expected *T*₇₅ at 150 cd m⁻² is 22.02 h (Figure S12, Supporting Information).

2.4. Optical Characteristics of Devices

The top-emitting structure offers increased light outcoupling and various optical benefits through the microcavity effect. The FWHM of the device was narrowed by adjusting the cavity length to match the main emission wavelengths of the QDs and the light reflected by the electrode under resonant conditions.^[19] Figure 4a shows the measured normalized angle-dependent EL intensity as a function of the ZMO thickness. The device with 45 nm-ZMO shows the most enhanced light emission at an emission angle of 0°. The devices with 55 and 65 nm-ZMO shows the highest luminance at angles other than the normal direction. This is because the cavity length of the device varies not only with the thickness of the functional layer (ZMO) but also with cos(Θ), depending on the viewing angle (Θ).^[79] From this, it can be considered that the angles at which the microcavity effect is maximized for each device are 0°, 30°, and 50°, respectively. The EQEs calculated based on this angular distribution are listed in Table 1. The EQE for the ZMO thicknesses of 45, 55, and 65 nm were calculated as 15.96%, 12.53%, and 4.75%, respectively. The highest light intensity angles for each device, confirmed at 0°, 30°, and 50°, respectively, indicate the angles at which resonant conditions occur for each device, resulting in improved color purity. Figure 4b–d illustrates the EL spectra of the three devices at 0°, 30°, and 50°, respectively. At the angle at which the light intensity exhibits a peak, it can be observed that the FWHM is narrowed by >8 nm compared to the FWHM of BQLED. This implies that the devices are improved in terms of both electrical efficiency and color purity.

3. Conclusion

In summary, we successfully achieved a uniform coating of a hydrophilic HIL on the Ag anode through solution processes via the introduction of a PEI interlayer, IPA doping of PEDOT:PSS, and dynamic spin-coating method. Furthermore, the interface of the formed anode composition exhibited an upshifted work function and bent energy levels, confirming the improvement in hole injection properties. Moreover, we

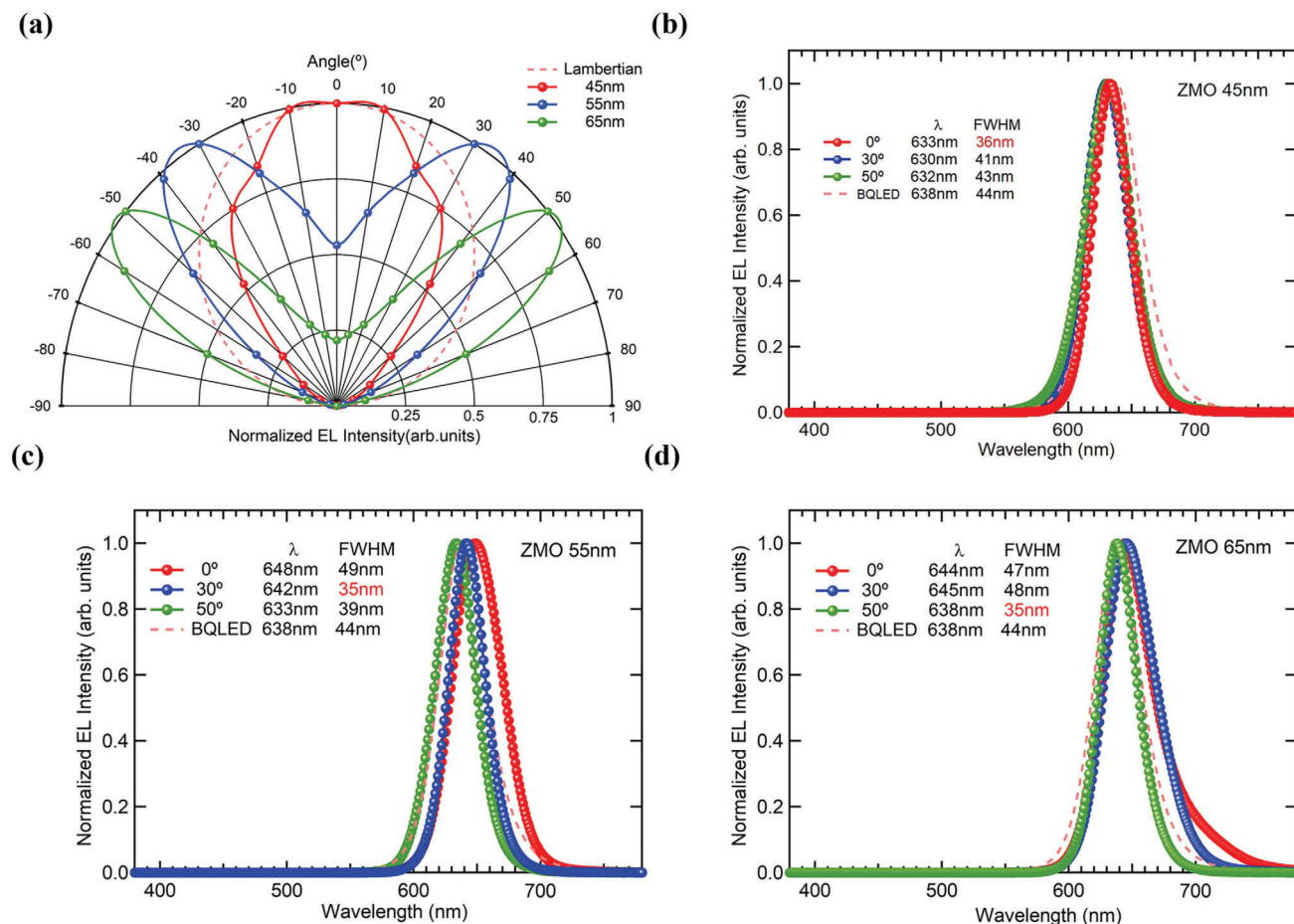


Figure 4. a) Measured normalized angle-dependent EL intensity. Normalized EL spectra at various viewing angles: b) 45 nm, c) 55 nm, and d) 65 nm.

fabricated all-solution-processable conventional TQLEDs. We controlled the cavity length by adjusting the thickness of the charge-transporting layers to maximize the microcavity effect at angles of 0°, 30°, and 50°. In particular, the device with a ZMO thickness of 45 nm exhibited a high current efficiency and power efficiency of 28.04 cd A⁻¹ and 7.38 cd W⁻¹, respectively, in the normal direction and a FWHM of 36 nm, marking the highest values in TQLED research using red InP QDs. We anticipate that our research, which has achieved electrical and optical advantages through an exclusively all-solution process, will contribute to the field of top-emissive QLEDs as a new device platform.

4. Experimental Section

Materials: Indium acetate (In(ac)₃, 99.99%), zinc acetate (Zn(Ac)₂, 99.99%), oleic acid (OA, 99%), 1-octadecene (ODE, ≥90%), tris(trimethylsilyl)phosphine ((TMS)₃P, 99.9%), n-triethylphosphine (TOP, 98%), selenium (Se, 99.9%), and sulfur (S, 99.9%) were purchased from Uniam. The Ag granule(4N) and Al pellet(5N) were purchased from iTASCO. Poly(3,4-ethylenedioxythiophene):poly(4-styrenesulfonate) (PEDOT:PSS, A14083) was purchased from Heraeus. Zinc acetate (Zn(Ac)₂, >99.9%) and magnesium acetate tetrahydrate (Mg(Ac)₂·4H₂O, 99%) were purchased from Alfa Aesar. Tetramethylammonium hydroxide pentahydrate (TMAH, >97%), poly[(9,9-dioctylfluorenyl-2,7-diyl)-co-(4,4'-(N-(4-sec-butylphenyl)diphenylamine))] (TFB), acetone, isopropyl alcohol

(IPA), ethanol, hexane, dimethyl sulfoxide, and chlorobenzene were purchased from Sigma–Aldrich.

Synthesis of InP core and InP/ZnSe/ZnS QDs: The InP/ZnSe/ZnS QDs were synthesized using previously reported methods, with minor modifications.^[80,81]

For a typical synthesis of InP cores, a mixture of 1.8 mmol of In(OA)₃ and 10 mL of ODE was loaded in a reaction flask and degassed at 110 °C for 1 h under vacuum. (TMS)₃P (1.5 mmol) diluted with TOP was injected into the flask, and the solution was subsequently heated to 280 °C for 30 min. Additional injections of 8 mmol of In(OA)₃ and 4.5 mmol of (TMS)₃P yielded larger InP cores. For the synthesis of InP/ZnSe/ZnS QDs, 1 mmol of Zn(OA)₂ and 10 mL of ODE were loaded in a reaction flask and degassed at 110 °C for 2 h. Upon filling up with nitrogen, InP (50 mg) core was injected into the flask at 180 °C. Subsequently, TOPSe (0.8 mmol) was added dropwise at 320 °C to grow a ZnSe shell. An additional ZnS shell was formed by adding Zn(OA)₂ and TOPS and allowed to react for 2 h. The reaction mixture was cooled to room temperature and purified.

Synthesis of ZMO NPs: ZnMgO nanoparticles were synthesized in the same manner as described in our previous report.^[74] TMAH solution (2187.6 mg in 30 mL of ethanol) was injected into a solution of Zn and Mg acetate (2041.4 mg of Zn acetate dihydrate and 150.1 mg of Mg acetate tetrahydrate dissolved in 60 mL of DMSO) and stirred for 2 h and 30 min. Subsequently, acetone was added to the mixed solution, which was allowed to stand for more than an hour until the particles settled. Following collection by centrifugation, the particles were dried and subsequently redispersed in a mixture of acetone, IPA, and hexane at a volume ratio of 1:1:4. The re-dispersed particles were subjected to another round

of centrifugation. The purification step was repeated after centrifugation. Finally, the purified ZnMgO nanoparticles were dispersed in ethanol.

Fabrication of Anode Composition: Glass substrates were cleaned with acetone, IPA, and deionized water in an ultrasonic cleaner, and stored in an oven at 100 °C overnight. The dried substrates were treated with UV-ozone for 15 min to remove any remaining organic residue and then transferred to a thermal evaporator to deposit the Ag anode (100 nm). Upon depositing the Ag, PEI in ethanol (0.5 mg mL⁻¹) was spin coated at 4000 rpm for 30 s, followed by annealing at 100 °C for 10 min. The substrates were then moved back to a fume hood to deposit the PEDOT:PSS. The substrates were pre-spun at 3000 rpm, and IPA-doped PEDOT:PSS stirred overnight was rapidly dispensed onto the rotating substrate (0.1–0.2 mL within 1 s) and spin-coated for 60 s. Finally, the substrates were annealed at 120 °C for 20 min. For the bottom-emitting QLEDs, pre-cleaned indium tin oxide (ITO, 150 nm)-patterned glass was cured by UV-ozone treatment for 15 min. Following UV-ozone treatment, the pristine PEDOT:PSS was spin-coated at 3000 rpm for 60 then annealed at 120 °C for 30 min.

Device Fabrication: The fabricated anode-HIL compositions were transferred to an N₂-filled glove box (<0.1 ppm H₂O) for device fabrication. The TFB in chlorobenzene (7 mg mL⁻¹) was spin-coated at 4000 rpm for 30 s then annealed at 150 °C for 30 min. Subsequently, the InP/ZnSe/ZnS QD in octane and ZnMgO in ethanol were spin-coated at 3000 and 4000 rpm, respectively, for 30 s and annealed at 70 °C for 30 min. Finally, the substrates were moved into a vacuum chamber to deposit 2 nm Al and 15 nm Ag cathode. All the metal electrodes were thermally evaporated at a rate of 1–2 Å s⁻¹ under 1.7 × 10⁻⁶ torr. The devices were encapsulated with a cover glass, except for the devices used to measure the angle-dependent EL intensity. For the bottom-emitting devices, 100 nm of Al was thermally evaporated at a rate of 1 Å s⁻¹ under 1.7 × 10⁻⁶ torr and was encapsulated with a cover glass.

Device Characterization: The J–V–L characteristics and EL spectra were measured using a CS-2000 spectroradiometer (Minolta) and source meter (Keithley 2450). The angle-dependent EL intensities were measured by rotating the stage on which the samples were mounted. The surface morphology was measured using AFM (XE-7). UPS spectra were recorded using a helium excitation source FC-XP10 (He 21.2 eV). High-resolution transmission electron microscopy (HR-TEM) was conducted using a JEM-2100F. The values of the refractive index (n) and extinction coefficient (k) of the materials constituting the layer for the optical simulation were measured using an M-2000D Ellipsometer. The contact angles were measured using a Phoenix-MT(A). The lifetime was measured using a lifetime test system (MC620S, McScience).

Optical Simulation: Optical simulations of the devices were performed using commercial software (SETFOS, Fluxim) based on the classical dipole mode.^[82] For the optical simulation, the n and k values of all functional layers, and the PL spectra of the QDs were used. In this simulation, it was assumed that the emitting molecules were isotropically oriented, the recombination zone was placed in the middle of the QD EML, and the intrinsic photoluminescence quantum yield was unity. Furthermore, the Purcell effect was considered to improve the calculation accuracy of the optical simulation, because the QLED was a top-emitting structure.^[83]

Supporting Information

Supporting Information is available from the Wiley Online Library or from the author.

Acknowledgements

This work was supported by the Basic Science Research Program (NRF-2022R1F1A1066526) through the National Research Foundation of the Ministry of Education, Republic of Korea. This research (for Hyunho Lee) was partially supported by the Basic Science Research Program through the National Research Foundation of Korea (NRF) funded by the Ministry of Education (no. 2018R1A6A1A03025242). This research was partly sup-

ported by a National Research Foundation (NRF) grant funded by the Ministry of Science and ICT (MSIT, Korea) (No. 2021R1F1A1045517) and (no. 2022R1A4A1028702), and an Institute of Information & Communications Technology Planning & Evaluation (IITP) grant funded by the MSIT (no. 2022-0-00026). The present Research has been conducted by the Research Grant of Kwangwoon University in 2023.

Conflict of Interest

The authors declare no conflict of interest.

Data Availability Statement

The data that support the findings of this study are available from the corresponding author upon reasonable request.

Keywords

indium phosphide, polyethylenimine, quantum dot light emitting diodes, solution processable, top emitting structure

Received: March 7, 2024

Revised: May 24, 2024

Published online:

- [1] V. L. Colvin, M. C. Schlamp, A. P. Alivisatos, *Nature* **1994**, 370, 354.
- [2] P. Yang, M. Ando, T. Taguchi, N. Murase, *J. Phys. Chem. C* **2011**, 115, 14455.
- [3] Y. Shirasaki, G. J. Supran, M. G. Bawendi, V. Bulović, *Nat. Photonics* **2013**, 7, 13.
- [4] Y. Yang, Y. Zheng, W. Cao, A. Titov, J. Hyvonen, J. R. Manders, J. Xue, P. H. Holloway, L. Qian, *Nat. Photonics* **2015**, 9, 259.
- [5] Z. Yang, M. Gao, W. Wu, X. Yang, X. W. Sun, J. Zhang, H.-C. Wang, R.-S. Liu, C.-Y. Han, H. Yang, *Mater. Today* **2019**, 24, 69.
- [6] B. Chen, D. Li, F. Wang, *Small* **2020**, 16, 2002454.
- [7] W.-C. Chao, T.-H. Chiang, Y.-C. Liu, Z.-X. Huang, C.-C. Liao, C.-H. Chu, C.-H. Wang, H.-W. Tseng, W.-Y. Hung, P.-T. Chou, *Commun. Mater.* **2021**, 2, 96.
- [8] H. Li, Y. Bian, W. Zhang, Z. Wu, T. K. Ahn, H. Shen, Z. Du, *Adv. Funct. Mater.* **2022**, 32, 2204529.
- [9] W. Zhang, Y. Tan, X. Duan, F. Zhao, H. Liu, W. Chen, P. Liu, X. Liu, K. Wang, Z. Zhang, *Adv. Opt. Mater.* **2022**, 10, 2200685.
- [10] C. W. Han, Y. H. Tak, *Flat Panel Display Manufacturing* **2018**, 143.
- [11] R. Zhu, Z. Luo, S.-T. Wu, *Opt. Express* **2014**, 22, A1783.
- [12] K. An, C. Kim, S. Kim, T. Lee, D. Shin, J. Lim, D. Hahm, W. K. Bae, J. Y. Kim, J. Kwak, *Small* **2023**, 19, 2206133.
- [13] S. Liu, W. Liu, W. Ji, J. Yu, W. Zhang, L. Zhang, W. Xie, *Sci. Rep.* **2016**, 6, 22530.
- [14] Y. J. Chen, W. K. Lee, Y. T. Chen, C. Y. Lin, S. W. Wen, M. Jiao, G. D. Su, H. Y. Lin, R. J. Visser, B. L. Kwak, *Adv. Sci.* **2018**, 5, 1800467.
- [15] S. Chen, L. Deng, J. Xie, L. Peng, L. Xie, Q. Fan, W. Huang, *Adv. Mater.* **2010**, 22, 5227.
- [16] S. D. Yambem, M. Ullah, K. Tandy, P. L. Burn, E. B. Namdas, *Laser Photonics Rev.* **2014**, 8, 165.
- [17] G. Liu, X. Zhou, S. Chen, *ACS Appl. Mater. Interfaces* **2016**, 8, 16768.
- [18] K. Y. Lai, S. Yang, T. C. Tsai, I. A. Yao, C. L. Yang, C. C. Chang, H. S. Chen, *Nanomaterials* **2022**, 12, 2683.
- [19] T. Lee, M. Lee, H. Seo, M. Kim, B. Chun, J. Kwak, *Small Methods* **2023**, 8, 2300266.
- [20] M. Park, Y. I. Kim, Y. K. Jung, J. g. Kang, S. Kim, J. Ha, Y. g. Yoon, C. Lee, *J. Soc. Inf. Display* **2022**, 30, 433.

- [21] C.-W. Chen, P.-Y. Hsieh, H.-H. Chiang, C.-L. Lin, H.-M. Wu, C.-C. Wu, *Appl. Phys. Lett.* **2003**, *83*, 5127.
- [22] H. Zhang, H. Li, X. Sun, S. Chen, *ACS Appl. Mater. Interfaces* **2016**, *8*, 5493.
- [23] C. Y. Lee, N. Naik Mude, R. Lampande, K. J. Eun, J. E. Yeom, H. S. Choi, S. H. Sohn, J. M. Yoo, J. H. Kwon, *ACS Appl. Mater. Interfaces* **2019**, *11*, 36917.
- [24] N. Li, T. Li, L. S. Li, J. Li, *Adv. Opt. Mater.* **2023**, *11*, 2300467.
- [25] C. Yi, D. Yoon, OLED Components and Materials, UBI Research, <https://ubiresearch.com/en/product/2023-oled-components-and-materials-report> (accessed: June 2023).
- [26] C. Yi, D. Yoon, OLED Emitting Materials, UBI Research, <https://ubiresearch.com/en/product/2023-oled-emitting-material-report> (accessed: May 2023).
- [27] J. Y. Oh, M. Shin, J. B. Lee, J.-H. Ahn, H. K. Baik, U. Jeong, *ACS Appl. Mater. Interfaces* **2014**, *6*, 6954.
- [28] Y. K. Chih, J. C. Wang, R. T. Yang, C. C. Liu, Y. C. Chang, Y. S. Fu, W. C. Lai, P. Chen, T. C. Wen, Y. C. Huang, *Adv. Mater.* **2016**, *28*, 8687.
- [29] F. E. Farina, W. S. Binti Azmi, K. Harafuji, *Thin Solid Films* **2017**, *623*, 72.
- [30] J. Vig, J. LeBus, *IEEE Trans. Parts Hybrids Packag.* **1976**, *12*, 365.
- [31] J. Kim, J. Wang, D. Daineka, E. V. Johnson, *Sol. Energy Mater. Sol. Cells* **2017**, *170*, 114.
- [32] S. Ding, W. Wang, X. Xiao, X. Qu, Z. Wu, B. Xu, S. Chen, K. Wang, X. W. Sun, *AIP Adv.* **2020**, *10*, 065308.
- [33] L. Chen, Z. Qin, S. Chen, *Small Methods* **2022**, *6*, 2101090.
- [34] L. Shi, S. Chen, *ACS Appl. Mater. Interfaces* **2022**, *14*, 30039.
- [35] J. Feng, M. Jiang, D. Li, Y. Zhang, C. Pei, L. Zhou, Z. Chen, Y. Li, X. Li, X. Xu, *J. Phys. Chem. Lett.* **2023**, *14*, 2526.
- [36] J. Qin, L. Lan, S. Chen, F. Huang, H. Shi, W. Chen, H. Xia, K. Sun, C. Yang, *Adv. Funct. Mater.* **2020**, *30*, 2002529.
- [37] M. Neophytou, F. Hermerschmidt, A. Savva, E. Georgiou, S. A. Choulis, *Appl. Phys. Lett.* **2012**, *101*, 193302.
- [38] S. Y. Lee, Y. S. Park, T.-Y. Seong, *J. Alloys Compd.* **2019**, *776*, 960.
- [39] R. Datta, N. Syed, A. Zavabeti, A. Jannat, M. Mohiuddin, M. Rokunuzzaman, B. Y. Zhang, M. Rahman, P. Atkin, K. Messalea, M. B. Ghasemian, E. Della Gaspera, S. Bhattacharyya, M. Fuhrer, S. Russo, C. F. McConville, D. Esraflizadeh, K. Kalantar-zadeh, T. Daenke, *Nat. Electron.* **2020**, *3*, 51.
- [40] J. W. Park, A. V. Takaloo, S. H. Kim, K. R. Son, D. Y. Kang, S. K. Kang, C. B. Lee, H. Choi, J. W. Shim, T. G. Kim, *J. Power Sources* **2021**, *489*, 229507.
- [41] H. Wang, C. Tang, Q. Shi, M. Wei, Y. Su, S. Lin, M. Dai, *Ceram. Int.* **2021**, *47*, 7666.
- [42] Y. Zhou, C. Fuentes-Hernandez, J. Shim, J. Meyer, A. J. Giordano, H. Li, P. Winget, T. Papadopoulos, H. Cheun, J. Kim, *Science* **2012**, *336*, 327.
- [43] K. Ding, H. Chen, L. Fan, B. Wang, Z. Huang, S. Zhuang, B. Hu, L. Wang, *ACS Appl. Mater. Interfaces* **2017**, *9*, 20231.
- [44] D. Kim, Y. Fu, S. Kim, W. Lee, K.-H. Lee, H. K. Chung, H.-J. Lee, H. Yang, H. Chae, *ACS Nano* **2017**, *11*, 1982.
- [45] Y. Fu, W. Jiang, D. Kim, W. Lee, H. Chae, *ACS Appl. Mater. Interfaces* **2018**, *10*, 17295.
- [46] S. Stolz, M. Scherer, E. Mankel, R. Lovrincic, J. Schinke, W. Kowalsky, W. Jaegermann, U. Lemmer, N. Mechau, G. Hernandez-Sosa, *ACS Appl. Mater. Interfaces* **2014**, *6*, 6616.
- [47] X. Yang, R. Wang, C. Fan, G. Li, Z. Xiong, G. E. Jabbour, *Org. Electron.* **2014**, *15*, 2387.
- [48] Y. Xuan, M. Sandberg, M. Berggren, X. Crispin, *Org. Electron.* **2012**, *13*, 632.
- [49] K. M. Kim, S. Ahn, W. Jang, S. Park, O. O. Park, D. H. Wang, *Sol. Energy Mater. Sol. Cells* **2018**, *176*, 435.
- [50] J. H. Lee, J. H. Heo, S. H. Im, O. O. Park, *ACS Appl. Mater. Interfaces* **2020**, *12*, 10527.
- [51] W. Zeng, L. Wang, X. Peng, T. Liu, Y. Jiang, F. Qin, L. Hu, P. K. Chu, K. Huo, Y. Zhou, *Adv. Energy Mater.* **2018**, *8*, 1702314.
- [52] L. Liu, S. Li, L. Wu, D. Chen, K. Cao, Y. Duan, S. Chen, *Org. Electron.* **2021**, *89*, 106047.
- [53] H. Shi, C. Liu, Q. Jiang, J. Xu, *Adv. Electron. Mater.* **2015**, *1*, 1500017.
- [54] J. Dong, G. Portale, *Adv. Mater. Interfaces* **2020**, *7*, 2000641.
- [55] H. Park, Y. Shi, J. Kong, *Nanoscale* **2013**, *5*, 8934.
- [56] E. Y. Choi, J. H. Seo, H. M. Kim, J. H. Kim, J.-T. Je, Y. K. Kim, 2010 3rd International Nanoelectronics Conference (INEC), IEEE, Piscataway, NJ, **2010**.
- [57] W. Lu, C. Wang, W. Yue, L. Chen, *Nanoscale* **2011**, *3*, 3631.
- [58] H.-C. Hsu, Y. Lai, W.-C. Hsieh, C.-F. Lin, *IEEE J. Photovoltaics* **2019**, *9*, 688.
- [59] F. Cao, D. Zhao, P. Shen, J. Wu, H. Wang, Q. Wu, F. Wang, X. Yang, *Adv. Opt. Mater.* **2018**, *6*, 1800652.
- [60] J. Wu, Y. Deng, X. Zhang, J. Xia, W. Lei, *Org. Electron.* **2018**, *58*, 191.
- [61] J. Wu, X. Zhang, J. Xia, W. Lei, B. Wang, *Org. Electron.* **2018**, *62*, 434.
- [62] Y. Fukuda, D. Abe, Y. Tanaka, J. Uchida, N. Suzuki, T. Miyai, Y. Sasanuma, *Polym. J.* **2016**, *48*, 1065.
- [63] Z. T. Gebremichael, C. Ugokwe, S. Alam, S. Stumpf, M. Diegel, U. S. Schubert, H. Hoppe, *RSC Adv.* **2022**, *12*, 25593.
- [64] C.-C. Lin, S. Gupta, C. Chang, C.-Y. Lee, N.-H. Tai, *Mater. Lett.* **2021**, *297*, 129941.
- [65] M. Tyona, *Adv. Mater. Res.* **2013**, *2*, 195.
- [66] R. S. N. Kumar, A. V. Ramirez, P. Verding, P. Nivelles, F. Renner, J. D'Haen, W. Deferme, *Commun. Eng.* **2023**, *2*, 42.
- [67] Y. Cun, C. Mai, Y. Luo, L. Mu, J. Li, L. Cao, D. Yu, M. Li, B. Zhang, H. Li, *J. Mater. Chem. C* **2020**, *8*, 4264.
- [68] X. Dai, Z. Zhang, Y. Jin, Y. Niu, H. Cao, X. Liang, L. Chen, J. Wang, X. Peng, *Nature* **2014**, *515*, 96.
- [69] M. K. Choi, J. Yang, D. C. Kim, Z. Dai, J. Kim, H. Seung, V. S. Kale, S. J. Sung, C. R. Park, N. Lu, *Adv. Mater.* **2018**, *30*, 1703279.
- [70] H. Shen, Q. Gao, Y. Zhang, Y. Lin, Q. Lin, Z. Li, L. Chen, Z. Zeng, X. Li, Y. Jia, *Nat. Photonics* **2019**, *13*, 192.
- [71] M. Yang, L. Xie, Y. Q. Yi, Y. Liu, X. Meng, W. Su, Z. Cui, *Adv. Mater. Technol.* **2023**, *8*, 2202105.
- [72] W. Zhang, X. Bi, X. Zhao, Z. Zhao, J. Zhu, S. Dai, Y. Lu, S. Yang, *Org. Electron.* **2014**, *15*, 3445.
- [73] C. N. Lungu, M. V. Diudea, M. V. Putz, I. P. Grudziński, *Int. J. Mol. Sci.* **2016**, *17*, 555.
- [74] D. Heo, J. H. Chang, D. Shin, J. Kwak, W. Bae, H. Lee, *Adv. Opt. Mater.* **2023**, *11*, 2202256.
- [75] B. Hwang, Y. Eun, G.-P. Jang, J.-H. Yang, M.-Y. Ha, D.-G. Moon, C. K. Kim, *Phys. Status solidi* **2022**, *219*, 2100856.
- [76] E. Staff, *Inf. Display* **2023**, *39*, 36.
- [77] W. Jin, Y. Deng, B. Guo, Y. Lian, B. Zhao, D. Di, X. Sun, K. Wang, S. Chen, Y. Yang, *npj Flex. Electron.* **2022**, *6*, 35.
- [78] H. Li, Y. Bian, W. Zhang, Z. Wu, T. K. Ahn, H. Shen, Z. Du, *Adv. Funct. Mater.* **2022**, *32*, 2204529.
- [79] Y. Fan, H. Zhang, J. Chen, D. Ma, *Org. Electron* **2013**, *14*, 1898.
- [80] D. Hahm, J. H. Chang, B. G. Jeong, P. Park, J. Kim, S. Lee, J. Choi, W. D. Kim, S. Rhee, J. Lim, *Chem. Mater.* **2019**, *31*, 3476.
- [81] B. G. Jeong, J. H. Chang, D. Hahm, S. Rhee, M. Park, S. Lee, Y. Kim, D. Shin, J. W. Park, C. Lee, *Nat. Mater.* **2022**, *21*, 246.
- [82] M. Furno, R. Meerheim, S. Hofmann, B. Lüssem, K. Leo, *Phys. Rev. B* **2012**, *85*, 115205.
- [83] H. Cho, J. Chung, J. Song, J. Lee, H. Lee, J. Lee, J. Moon, S. Yoo, N. S. Cho, *Opt. Express* **2019**, *27*, 11057.